Voltage-Driven Fluorine Motion for Novel Organic Spintronic Memristor

Abir Nachawaty, Tongxin Chen, Fatima Ibrahim, Yuchen Wang, Yafei Hao, Kevin Dalla Francesca, Priyanka Tyagi, Antonio Da Costa, Anthony Ferri, Chuanchuan Liu, et al.

Title: Voltage-driven fluorine motion for novel organic spintronic memristor

Abir Nachawaty⁂, Tongxin Chen⁂, Fatima Ibrahim⁂, Yuchen Wang⁂, Yafei Hao⁂, Kevin Dalla Francesca, Priyanka Tyagi, Antonio Da Costa, Anthony Ferri, Chuanchuan Liu, Xiaoguang Li, Mairbek Chshiev, Sylvie Migot, Laurent Badie, Walaa Jahjah, Rachel Desfeux, Jean-Christophe Le Breton, Philippe Schieffer, Arnaud Le Pottier, Thomas Gries, Xavier Devaux, Yuan Lu**

⁂Authors having equal contributions

Dr. Abir Nachawaty, Dr. Tongxin Chen, Prof. Yafei Hao, Dr. Priyanka Tyagi, Dr. Sylvie Migot, Dr. Laurent Badie, Dr. Thomas Gries, Dr. Xavier Devaux*, Dr. Yuan Lu*

Institut Jean Lamour, CNRS-Université de Lorraine, UMR 7198, 54011 Nancy, France

Email: yuan.lu@univ-lorraine.fr; xavier.devaux@univ-lorraine.fr

Dr. Fatima Ibrahim, Prof. Mairbek Chshiev

Université Grenoble Alpes, CEA, CNRS, SPINTEC, Grenoble 38000, France

Yuchen Wang, Chuanchuan Liu, Prof. Xiaoguang Li

Hefei National Laboratory for Physical Sciences at the Microscale, Department of Physics, University of Science and Technology of China, Hefei 230026, China

Dr. Kevin Dalla Francesca, Dr. Antonio Da Costa, Dr. Anthony Ferri, Prof. Rachel Desfeux

Univ. Artois, CNRS, Centrale Lille, Univ. Lille UMR 8181, Unité de Catalyse et Chimie du Solide (UCCS), F-62300 Lens, France

This article has been accepted for publication and undergone full peer review but has not been through the copyediting, typesetting, pagination and proofreading process, which may lead to differences between this version and the Version of Record. Please cite this article as doi: 10.1002/adma.202401611.

Dr. Walaa Jahjah, Dr. Jean-Christophe Le Breton, Prof. Philippe Schieffer, Arnaud Le Pottier

Univ. Rennes-CNRS, IPR (Institut de Physique de Rennes)-UMR 6251, F-35000 Rennes, France

Prof. Yafei Hao

Physics Department, Zhejiang Normal University, Zhejiang 321004, China

Keywords: Tunneling magnetoresistance; Memristor; Neuromorphic computation; Poly(vinylidene fluoride); Langmuir-Blodgett.

Integrating tunneling magnetoresistance (TMR) effect in memristors is a long-term aspiration because it allows to realize multifunctional devices, such as multi-state memory and tunable plasticity for synaptic function. However, the reported TMR in different multiferroic tunnel junctions is limited to 100%. Here, we demonstrate a giant TMR of -266% in $La_{0.6}Sr_{0.4}MnO_3$(LSMO)/poly(vinylidene fluoride)(PVDF)/Co memristor with thin organic PVDF barrier. Different from the ferroelectricity-based memristors, we discover that the voltage-driven F motion in the junction generates a huge reversible resistivity change up to 10^6% with *ns* timescale. The removing F from PVDF layer suppresses the dipole field in the tunneling barrier, thereby significantly enhances the TMR. Furthermore, the TMR can be tuned by different polarizing voltage due to the strong modification of spin-polarization at the LSMO/PVDF interface upon F doping. The combining of high TMR in the organic memristor paves the way to develop high-performance multifunctional devices for storage and neuromorphic applications.

1. Introduction

Memristor[1] have garnered significant interest over the past decade due to their potential applications, such as non-volatile memory[2], neuromorphic and bio-inspired computing[3,4], and threshold logic[5]. Various physical mechanisms have been proposed to realize memristive properties, particularly the reversible transition between the high resistance state and the low resistance state. These mechanisms include the migration of oxygen vacancies[6,7], the formation of metallic filaments[8,9] or agglomeration[10] inside the active layer, charging or discharging of nanoparticles in the conduction channel[11], metal substitution in 2D materials[12,13], ferroelectricity of tunnel barriers[14,15,16], and magnetic domain motion in magnetic tunnel junctions (MTJs)[17].

Combining the tunnel magnetoresistance (TMR) effect with memristors allows the creation of new multifunctional devices. The change in resistance not only depends on the memristive mechanism but also relies on the magnetization configurations of the electrodes. For example, it can generate multi-level memories to significantly increase the storage capacity[18,19]. Additionally, TMR can provide a new degree of freedom to control the plasticity characteristics of the memristor-based artificial synapse[16], which is crucial for emulating the synaptic morphological alteration property in a biological synapse. To date, most TMR combined memristors have been realized through multiferroic tunnel junctions (MFTJs)[20], where a ferroelectric barrier is sandwiched between two ferromagnetic electrodes. However, the interface spin-polarization[21] can be strongly influenced by the magneto-electric coupling at the interface and the large dipole and dielectric field inside the barrier, so that the reported TMR ratio is still small and limited to 100%[22].

In this work, we have demonstrated a significant TMR enhancement up to -266% in a $La_{0.6}Sr_{0.4}MnO_3$ (LSMO)/poly(vinylidene fluoride) (PVDF)/Co memristor with a thin organic PVDF barrier fabricated by the Langmuir-Blodget (LB) method. Generally, PVDF and its copolymers are well-known for their superior ferroelectric properties[23] due to the formation of dipoles between

positively charged hydrogen ions (H^+) and the negatively charged fluorine ions (F^-)[24]. However, in this work, we have discovered a novel memristive mechanism different than the previously reported ferroelectricity-induced memristor effect[25,26]. We find that F components can be significantly decomposed from the thin PVDF layer after the annealing at 120°C on the LSMO electrode. Upon the polarizing voltage applied to the junction, the F components can be driven either to the LSMO/PVDF interface or into the top Co layer, reversibly changing the junction resistivity by more than 10^6% with *ns* timescale. The voltage-driven F motion not only creates a substantial memristor effect but also strongly modifies the interface spin-polarization, resulting in a change in TMR sign and amplitude. The removal of F from the PVDF barrier can also explain the reason for the TMR enhancement. The giant TMR in the organic spintronic memristor has great potential for realizing multifunctional devices for storage and neuromorphic applications.

2. Results and discussions

2.1 Demonstration of voltage-driven fluorine motion in LSMO/PVDF/Co junctions

Our junction comprises the following structure: $SrTiO_3$ substrate//LSMO (50 nm)/PVDF (5 layers)/Co (10 nm)/Au (10 nm). The fabrication details are provided in **Experimental Section/Methods**. The five-layer PVDF film was deposited using the LB method in a vertical dipping mode, which is more suitable for fabricating sub-10 nm ultrathin layers[27] than the spin-coating method[28]. We utilized high-resolution scanning transmission microscopy (HR-STEM) to characterize the interfacial structures. Since atomic force microscopy (AFM) characterization revealed that the PVDF barrier is not homogeneous due to the incomplete coverage of PVDF on LSMO (refer to **Supporting Information (SI) Note 1**), STEM characterization was focused on the thinnest PVDF region, where the tunneling transport is

expected to occur. **Figure 1a** displays a large-scale HR-STEM high-angle annular dark-field (HAADF) image, clearly delineating the LSMO, PVDF, and Co/Au layers. In the magnified HAADF image (**Fig. 1b**), the thickness of PVDF varies from 2 to 5 nm. The roughness of PVDF is primarily associated with the roughness of the LSMO electrode, exhibiting a peak-to-peak height of 1-2 nm.

To demonstrate voltage-driven F motion in the LSMO/PVDF/Co junction, we conducted spatially-resolved electron energy loss spectroscopy (EELS) to analyze the chemical distribution within the junction structure. Two junctions from the same sample were polarized in opposite directions before being processed into lamella STEM samples. **Figs. 1d-h** display the EELS elemental maps of the positively polarized junction, while **Figs. 1j-n** show the negatively polarized one. Apart from the inherent oxygen in the LSMO layer, an additional oxygen distribution (**Fig. 1f,l**) is observed above the PVDF layer (depicted by the carbon (C) signal in **Fig. 1d,j**). This oxygen signal is likely due to the water or air contamination on the PVDF surface introduced during the LB fabrication process. The presence of oxygen cannot be entirely removed even after annealing at 120°C under vacuum. Consequently, the Co on PVDF undergoes partial oxidation (approximately 1.2 nm). Upon comparing **Figs. 1d,j** and **Figs. 1f,l**, it is evident that the oxidized Co layer uniformly follows the morphology of the PVDF layer. Interestingly, the locations of the F and C signals do not overlap, indicating that PVDF has completely decomposed, and F atoms have been driven out of the PVDF layer. The F elements either move towards the LSMO side in the junction after positive polarization (**Fig. 1e**) or enters the Co side after negative polarization (**Fig. 1k**). In **Figs. 1k** and **1l**, the F signal almost overlaps with the additional O signal, suggesting that all fluorine contents have migrated entirely into the oxidized Co layer.

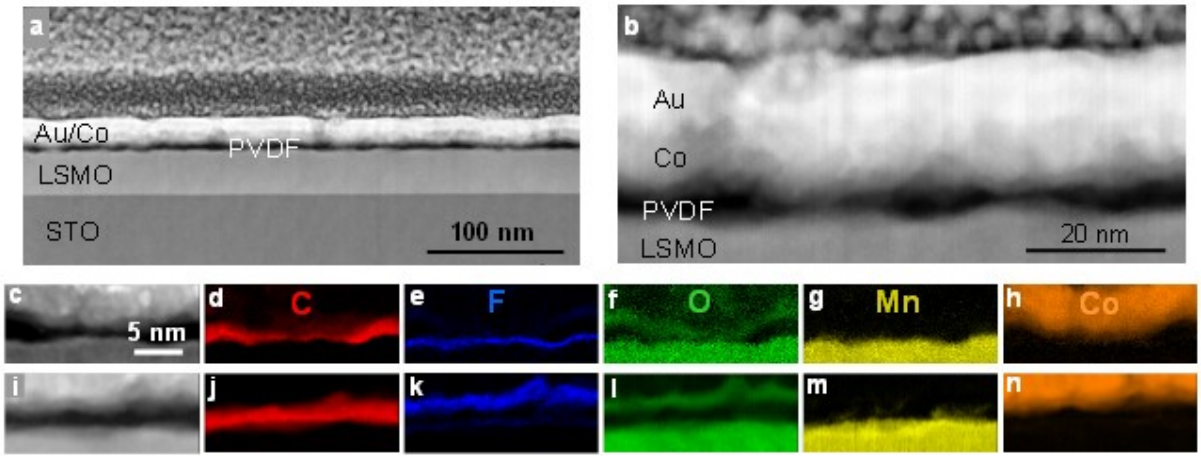

Figure 1. Demonstration of voltage-driven fluorine motion in LSMO/PVDF/Co junctions. a) Large-scale high-resolution scanning transmission microscopy (HR-STEM) high-angle annular dark-field (HAADF) image displaying the multilayer structure. b) Enlarged HAADF image showing the thin PVDF barrier. c,i) HAADF images of the two junctions from the same sample. One is after positive polarization (c) and the other is after negative polarization (i). **d-h,** Spatially-resolved electron energy loss spectroscopy (EELS) elemental maps were generated from the zone shown in **c** for the positively polarized junction. j-n) EELS elemental maps were generated from the zone shown in (i) for the negatively polarized junction. Chemical maps were drawn by processing EELS spectrum images using the signals of C_K (287 eV) (d,j), F_K (688 eV) (e,k), O_K (532 eV) (f,l), $Mn_{L3\text{-}2}$ (641 eV) (g,m), and $Co_{L3\text{-}2}$ (779 eV) (h,n). Remarkably, the location of F and C signals do not overlap, indicating that PVDF has been completely decomposed, and F atoms have been driven out of the PVDF layer. The F element either moves towards the LSMO side after positive polarization (e) or enters the Co side after negative polarization (k).

2.2 Magneto-transport characterizations of LSMO/PVDF/Co junctions

To investigate magneto-transport properties, we initially fabricated the junction device using an *in-situ* mask technique. **Fig. 2a** illustrates the schematic structure of the LSMO/PVDF/Co junction on a $SrTiO_3$ (STO) substrate. The inset of **Fig. 2a** showcases one of the junction devices, approximately 200×200 μm^2 in size. In order to demonstrate the memristor effect, we measured the resistance of the junction after applying different polarizing voltages. **Fig. 2b** depicts two successive cycles of resistance *vs.* polarizing voltage, clearly presenting a high resistance state (HRS, R_H) and a low resistance state (LRS, R_L). The second cycle reproduces HRS and LRS with a narrower coercivity voltage (~1.2 V) compared to the first cycle (~1.6 V), indicating a history-dependent polarization

behavior, which will be discussed further below. In comparison to the tunneling electroresistance (TER) associated with the ferroelectric tunnel junctions, we define the resistance change ratio (RCR) as $(R_H\text{-}R_L)/R_L\times100\%$, which can reach up to 4300%. This is nearly two orders of magnitude larger than the TER of 75% reported in previous LSMO/PVDF/Co MFTJ with ferroelectric mechanism[28]. To assess the retention of resistive switching, we conducted 100 cycles of alternate +1.8 V and -2.0 V polarizations on the junction, as demonstrated in **Fig. 2c**. Both resistance states are well preserved after 100 polarization cycles. For further details regarding the retention measurements, please refer to **SI Note 2**.

We also conducted TMR measurements on the thin PVDF junctions. Prior to any polarization, the junction exhibits a TMR of +4.2% (refer to **SI Note 3**). Following positive polarization, the TMR maintains a similar amplitude of +5% in the HRS (**Fig. 2d**). However, after appropriate negative polarization in the LRS, we measured a remarkably large TMR, reaching -120% (**Fig. 2e**). The distinct resistance plateaus observed between 50 to 400 G and -80 to -700 G indicate a well-defined antiparallel (AP) magnetic configuration between the LSMO and Co electrodes. Typically, the TMR is lower than 30-40% for micrometer-sized organic MTJs fabricated using an *in-situ* mask technique, as reported in previous studies[29,30]. In our case, the observed TMR is nearly one order of magnitude higher than the previously reported TMR (-15%) in PVDF based MFTJ by spin-coating method[28,31] (see detailed comparison in **SI Note 4**). The remarkably high TMR (-120%) is surprising, especially considering the large size of the junction ($200\times200\ \mu m^2$) and the presence of an inhomogeneous PVDF barrier. The high resistance of the junction in the LRS (hundreds of kΩ) indicates that transport does not occur across the entire junction surface but is limited to

a small region where the barrier is thinnest. For additional bias and temperature-dependent characterizations, please refer to **SI Note 5**.

We observed that the TMR is sensitive to the cyclic polarization. Following 100 cycles of polarization, the TMR in the LRS decreases from the initial -120% to -8% (**Fig. 2f**). However, a partial recovery of the TMR to -28% is achieved after applying a higher negative polarizing voltage (-2.4 V). To understand this phenomenon, we characterized the junction after cyclic polarization using STEM-EELS (refer to **SI Note 6**). Despite a significant portion (75%) of the F element being distributed in the CoO layer, a minor fraction (25%) of F still resides at the LSMO/PVDF interface. This presence effectively reduces the interface spin-polarization (see below *ab-initio* calculation) and results in the significant decline in TMR. Consequently, a higher polarizing voltage is necessary to drive the residual F element away from the LSMO side, facilitating the TMR recovery. Careful adjustment of the polarization voltage enables precise control of F distribution at both interfaces, ensuring the reproducibility in the resistivity switching and achieving the desired TMR ratio.

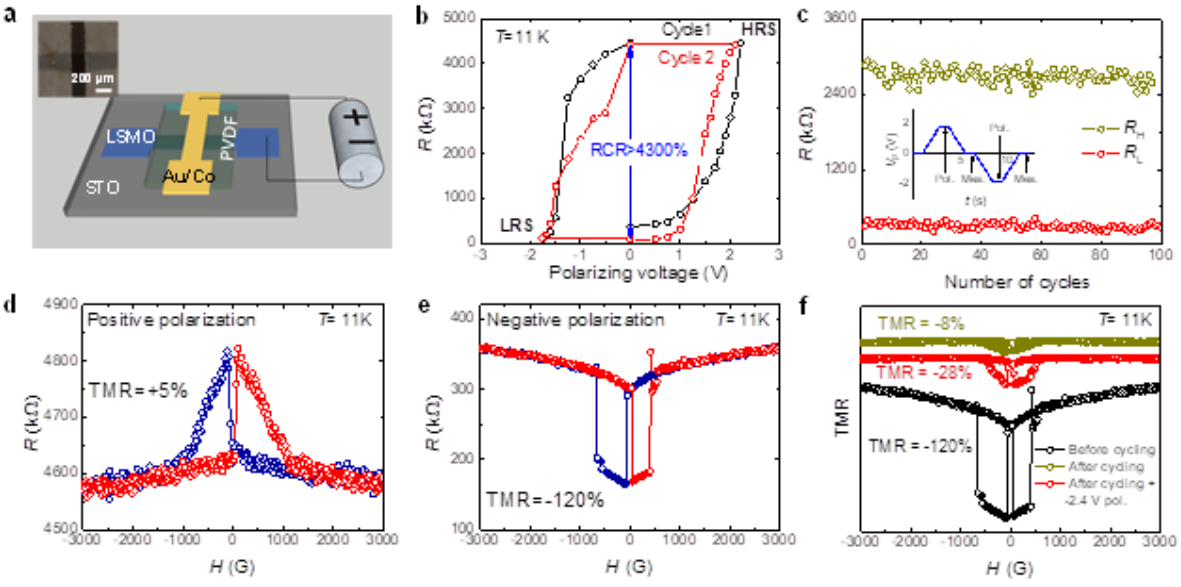

Figure 2. Magneto-transport measurements on LSMO/PVDF/Co devices fabricated with an *in-situ* mask. a) Schematics illustrating the structure and measurement setup of the LSMO/PVDF/Co/Au

device. Inset: Optical image of the junction with dimensions of 200×200 μm^2. b) The first two successive loops of resistance *vs.* polarizing voltage on the same junction. Resistance was measured under V_{mes}=+10 mV. c) Display of 100 cycles of resistive switching. Resistance was measured after each polarizing with V_P=+1.8 V (dark yellow) and V_P=−2.0 V (red), respectively. Inset: Diagram illustrating the polarization voltage on the junction for one cycle of polarization. d) Tunneling magnetoresistance (TMR) measured under V_{mes}=+10 mV at T=11 K after positive polarization with V_P=+2.1 V. e) TMR curves measured after negative polarization with V_P=-1.9 V. f) TMR curves before cyclic polarization (black), after cyclic polarization (dark yellow) and after cycling plus -2.4 V polarization (red).

2.3 Giant TMR and synaptic function in small size junctions

To further optimize the device performance, we developed a UV lithography technique to fabricate smaller junctions, achieving dimensions as small as 5×5 μm^2 (Inset in **Fig. 3a**). Remarkably, after proper negative polarization, the junctions with a thinner barrier (3 layers of PVDF) exhibit significantly higher TMR, reaching up to -266% (**Fig. 3b**). In fact, the spin diffusion length in the ferroelectric PVDF barrier is much smaller (7.2 nm at 20 K)[32] compared to those reported in non-ferroelectric organic barriers such as Alq_3 (45 nm at 10 K)[33] and P(NDI2OD-T2) (64.5 nm at 4.2 K)[34]. This normally should result in a considerably lower TMR in the LSMO/PVDF/Co junction compared to the LSMO/Alq_3/Co junction. However, the measured high TMR suggests a notably increased spin diffusion length in the PVDF barrier after the removal of F. This enhancement is likely attributed to the elimination of the dipole or dielectric fields within the PVDF layer, resulting in the reduced electron scattering within the barrier and consequently an enhanced spin diffusion length. Furthermore, decreasing the junction size effectively promotes the junction homogeneity, further amplifying the TMR ratio.

Additionally, we conducted measurements of resistance *vs.* polarizing voltage loops for the junction using various pulse widths (**Fig. 3c**). The measuring voltage (V_{mes}) was set at +0.2 V. Surprisingly, we have observed a significant enhancement in RCR in the small junctions, reaching up to 10^6% with 10 μs pulsed polarization. Even with 20 ns pulse width,

we still achieve a RCR of 10^5%. It is found that longer pulse duration than 10 μs has very little effect on the RCR. The shape of the loop remains almost unchanged as the pulse width reduces to 100 ns. However, below 100 ns, the LRS resistance starts to increase, leading to a reduction in RCR. We found that the shape of the pulsing voltage is significantly altered below 100 ns due to the impedance mismatch in our electric circuit (refer to **SI Note 7**), effectively diminishing the polarization efficiency. Nevertheless, the rapid polarization indicates that the motion speed of F element can exceed at least 0.1 m/s by crossing the PVDF barrier within the limitations of our setup. This speed is notably faster than the previously reported ionic motion speeds in other non-organic ionic devices[35,36]. We have compared the performance of our memristor with other state-of-art MFTJs where the memristive mechanism is due to the ferroelectricity of tunneling barrier (see **SI Note 8**).

In addition to showcasing the bipolar switching characteristics, we also demonstrate the capability to tune the resistance of the memristor continuously by adjusting the polarity of the applied programming voltage. **Fig. 3d** presents the results when the junction is polarized using a series of positive (+1 V, 10 ms) and negative (-1 V, 10 ms) pulses. The positive voltage pulses progressively elevate the junction resistance, whereas the negative pulses reduce the resistance. This mimics synaptic potentiation and depression processes. Moreover, due to the interplay of the TMR effect, the resistance displays distinct responses for parallel and antiparallel magnetization configurations. This effect suggests the potential of utilizing an external magnetic field to modulate the synaptic response[16].

Spike-timing-dependent plasticity (STDP) is a crucial mechanism in competitive Hebbian learning, enabling adjustments in synaptic weight based on the precise timing of pre- and postsynaptic spikes[4]. We emulate the STDP function in our memristor by applying a

voltage waveform depicted in the upper panel of **Fig. 3e**, simulating the activities of pre- and postsynaptic neurons (V_{pre} and V_{post}). The waveform comprises a rectangular voltage pulse followed by a smooth slope of the opposite polarity, carefully controlled to ensure the voltage never exceeds the threshold voltage (V_{th}), thus preventing a single spike from altering the resistance. When both pre- and post-neuron spikes reach the memristor with a delay Δt, the resulting combined waveform temporarily surpasses V_{th} (Insets of lower panel of **Fig. 3e**). This leads to either an increase ($\Delta G>0$, strengthening) or a decrease ($\Delta G<0$, weakening) in synaptic connectivity, with the weight change ($\Delta G/G$) depending on the sign of Δt. As depicted in the lower panel of **Fig. 3e**, for $\Delta t>0$ ($\Delta t<0$), the synaptic weight undergoes augmentation (diminution), representing long-term potentiation (depression) characters. Our findings closely align with other studies[15,16], illustrating that only closely timed spikes induce a conductance change, while prolonged delays do not alter the conductivity. The successful replication of these biological synaptic functions underscores the high potential of our organic memristor for integration into artificial neural systems.

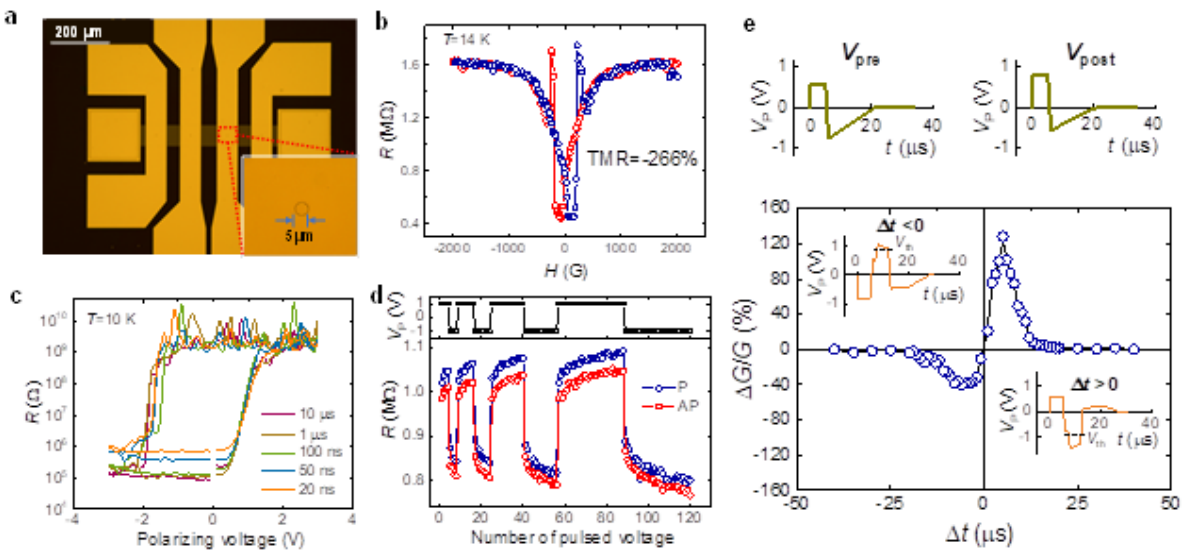

Figure 3. Giant TMR and synaptic function measurements on LSMO/PVDF/Co devices fabricated by UV lithography. a) Optical image of LSMO/PVDF/Co/Au device fabricated by UV lithography. Inset: Magnified optical image displaying one junction with dimensions of 5×5 μm^2. b) TMR curves measured under V_{mes}=+10 mV at T=14 K after negative polarizing with V_P=-1.6 V. c) Resistance *vs.* polarizing voltage loops with different pulse widths. Resistance was measured under V_{mes}=+0.2 V at T=10 K. d) Evolution of junction resistance (lower panel) as a function of a series of n identical positive pulses (+1 V, 10 ms) followed by n identical negative pulses (-1 V, 10 ms), with n exponentially increasing from 4 to 32 (upper panel). The junction resistance exhibits a different response when the magnetization configuration is in parallel (P) and antiparallel (AP) states. e) Upper panel: Pre- and postsynaptic spikes with a total length of 20 μs. The amplitudes of the rectangular voltage pulse and opposite slope are +0.6 V and -0.75 V for the spike from presynaptic neuron, and +0.8 V and -0.55 V for the spike from postsynaptic neuron, respectively. Lower panel: Measurements of spike-timing-dependent plasticity (STDP) at 10 K. The ratio of device conductance change ($\Delta G/G$) as a function of the delay (Δt) between pre- and postsynaptic spikes. Insets: Waveforms resulting from the superposition of pre- and postsynaptic spikes.

2.4 *Ab-initio* analyses of spin polarization with F incorporation

To unveil the origin of the polarization-dependent TMR effect, we performed *ab-initio* calculations, considering four distinct possible interfaces corresponding to the experimental cases (see **Experimental Section/Methods**). For positive polarization, the first interface entails F atoms inserted at the LSMO/C-H chains interface (**Fig. 4a**), while the other interface comprises bare C-H chains/CoO (**Fig. 4c**). In the case of negative polarization, the first interface is modeled with bare LSMO/C-H chains (**Fig. 4e**), and the second interface involves C-H chains/CoO with the incorporation of F atoms (**Fig. 4g**). For simplicity, we employed C-H chains to simulate the PVDF after F decomposition. It is found that the C-H chains possess a large band gap (~5.5 eV), akin to that of the PVDF chains. Consequently, we attribute any states within this gap as interface states induced by the magnetic electrodes (either LSMO or CoO). It is known that when organic molecules come into contact with a ferromagnetic metal, hybridization between the molecular orbitals and the spin-split bands of the ferromagnet gives rise to the "spinterface", exhibiting highly efficient spin-filtering properties[28,37]. To

explore the potential of these C-H chains in spin filtering of tunneling electrons, **Figs. 4b,d,f,h** display the spin-resolved density of states (DOS) projected on the carbon atoms and the corresponding spin polarization (P_s) for each interface. We observe that P_s highly depends on the placement of the F atoms. When F is inserted into LSMO under positive polarization, we observe a low P_s of approximately +9% (**Fig. 4b**). However, upon removing F under negative polarization, a high P_s of nearly +100% is achieved (**Fig. 4f**), reflecting the half-metallicity of the bare LSMO. On the other side, inserting F into CoO under negative polarization results in a negative P_s of about -15% (**Fig. 4h**), while P_s changes to approximately +48% after removing the F atoms (**Fig. 4d**). By considering the Jullière formula for tunneling between two FM electrodes[38], we can estimate a positive (negative) TMR sign for positive (negative) polarization conditions, respectively, which qualitatively aligns with the aforementioned observed TMR values (+5% and -120%) for different polarization states. The sign change of spin-polarization at the PVDF/CoO interface with/without F incorporation explains the observed TMR sign change. The rapid decrease in TMR under positive polarization is attributed to the reduction in spin-polarization at the LSMO/PVDF interface due to the F insertion.

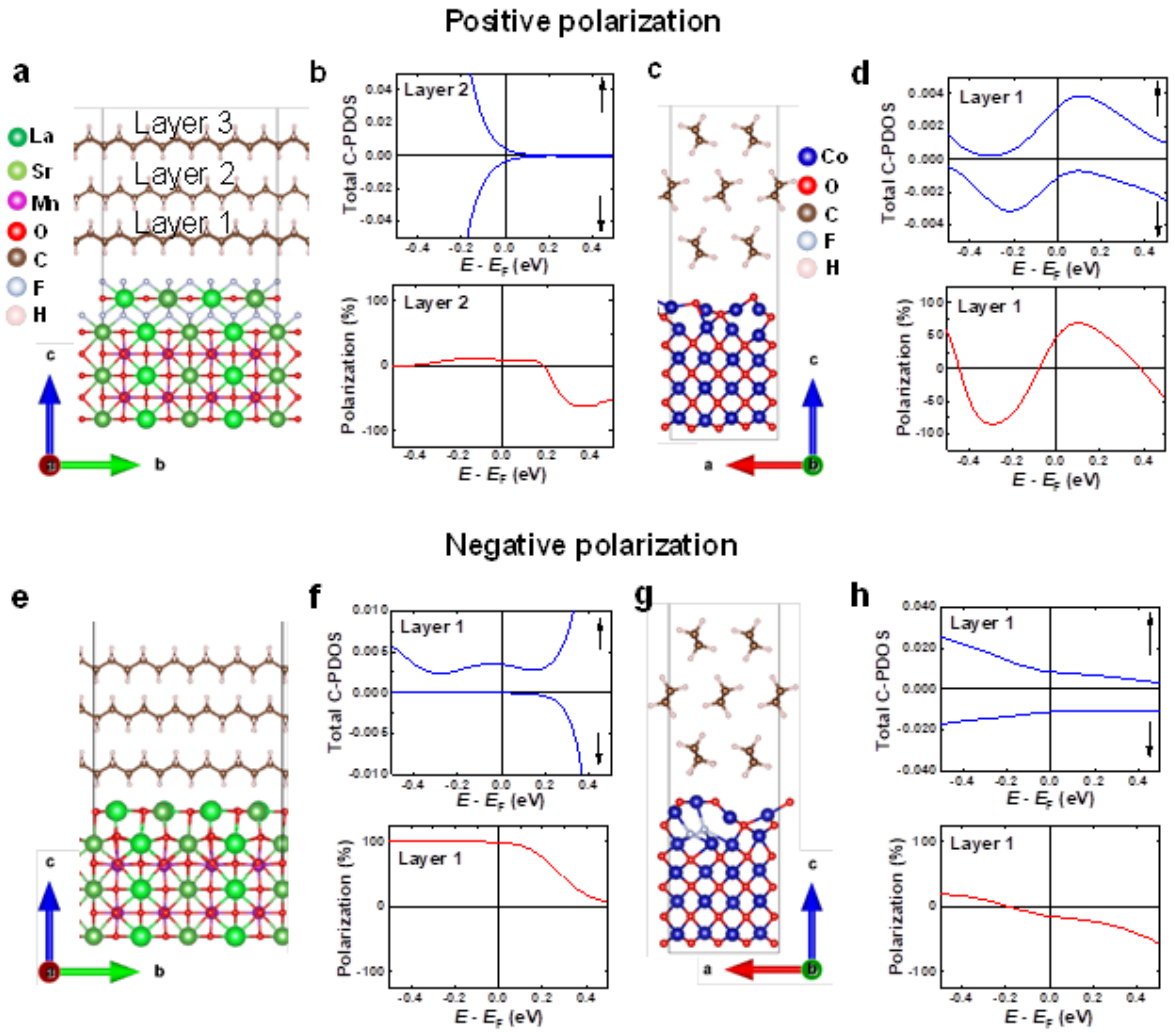

Figure 4. *Ab-initio* calculations of spin-polarization at four interfaces in LSMO/PVDF/Co structure under different polarizations. a,e) Supercells of LSMO:F/C-H chains (a) and bare LSMO/C-H chains (e). b,f) Spin-dependent carbon-projected density of states (C-PDOS) and the spin-polarization plotted for LSMO:F/C-H chains (b) and bare LSMO/C-H chains (f), respectively. c,g) Supercells of bare CoO/C-H chains (c) and CoO:F/C-H chains (g). d,h) Spin-dependent C-PDOS and the spin-polarization for bare CoO/C-H chains (d) and CoO:F/C-H chains (h), respectively. a-d) correspond to the interfaces under positive polarization. e-h) correspond to the interfaces under negative polarization.

2.5 Mechanism of memristive effect

To comprehend the memristive effect associated with the F motion, we conducted *I-V* characterizations at various temperatures for both polarization states (**SI Note 9**). By

employing the Brinkman model to fit the *I-V* curves[39], we extracted parameters such as barrier thickness, height, and asymmetry. The two resistance states exhibited distinct barrier thicknesses, with the HRS having a thickness about 0.8 nm larger in the low-temperature range (<100 K). Considering that F insertion in LSMO was observed in the HRS, one might hypothesize that LSMO doping with F may create an additional tunneling barrier. However, *ab-initio* calculations reveal that the DOS at the interface of LSMO:F/C-H chains is significantly enhanced due to the F insertion (**SI Note 10**), which also results in the reduction of interface spin-polarization. Therefore, attributing the increase in barrier thickness to the F insertion into LSMO is not appropriate. Another possibility could be the alteration in resistivity in the CoO layer due to the F incorporation. As previously reported, CoO is a semiconductor with a band gap of approximately 2.2-2.8 eV[40,41], consistent with our *ab-initio* calculations (~2 eV). Nevertheless, F doping in CoO introduces strong states in the band gap at the Fermi level (**SI Note 11**), elucidating the observed reduction in resistivity under negative polarization. Under positive polarization, the F atoms are driven towards LSMO, restoring the resistivity of CoO and re-establishing the additional tunneling barrier. In **Fig. 5**, we present schematics illustrating the change in barrier thickness under different polarization states. This explanation also accounts for the disparate temperature dependencies outlined in **SI Note 5**. The rapid decline in resistance in the HRS signifies a characteristic of hopping transport through a thick tunneling barrier[42]. Furthermore, we have performed the capacitance-voltage (*C-V*) measurements in our LSMO/PVDF/Co junction sample fabricated by *in-situ* mask (**SI Note 12**). The *C-V* characteristic observed in our junction prepared by the LB method, is entirely distinct from the "butterfly" pattern observed in typical ferroelectric PVDF. These findings undeniably confirm that the decomposed thin PVDF layer in our

junction no longer exhibits ferroelectric properties. We observed a character of *C-V* hysteresis loop with clear two-level capacitance dependent on the applied voltage, which is well consistent with the resistivity switching mechanism attributed to the change in tunneling barrier thickness induced by the F motion.

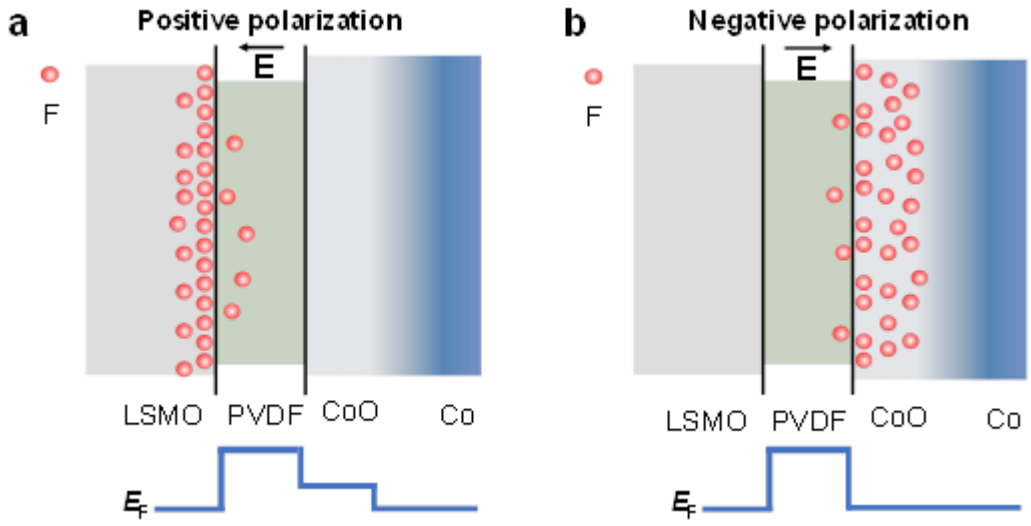

Figure 5. Mechanism of the memristive effect. a,b) Schematics illustrating the change in the barrier thickness under positive polarization (a) and negative polarization (b). With voltage-controlled F motion, the barrier thickness is considered to be a sum of PVDF and CoO layers under positive polarization, while only the PVDF layer is considered as the tunneling barrier under negative polarization due to the reduction of CoO resistivity with F insertion.

2.6 Mechanisms for voltage-driven fluorine motion

Several possibilities could potentially lead to the dissociation of F from the PVDF layer, including the polarizing voltage, Co/Au deposition, or the LSMO bottom layer. To elucidate the underlying origin, we have examined the interface structure and chemistry of the PVDF film on LSMO without Co/Au deposition. Our observations reveal a significant concentration of F on the surface of LSMO, whereas the F concentration was notably reduced near the PVDF/LSMO interface (see **SI Note 13** for details). In addition, by performing piezo-

response force microscopy (PFM) on the PVDF/LSMO sample, we have discovered a strong degradation of PVDF ferroelectricity upon applying a positive voltage from the tip (see **SI Note 13**) when F atoms are driven into LSMO. All evidence indicates that the PVDF undergoes an initial decomposition by the LSMO substrate even before Co/Au deposition. LSMO is known to contain oxygen vacancies, particularly on its surface[43], depending on the growth process[44]. This characteristic could trigger the fluorination of LSMO and the subsequent decomposition of PVDF during the 120°C annealing procedure.

Upon the application of a polarizing voltage, the decomposed F is driven towards different interfaces, resulting in the significant memristive effect. There are several possible mechanisms to describe this voltage-driven F motion. Firstly, it could involve the motion of negative F^- ions, similar to the reversible magnetization tuning demonstrated in Ruddlesden-Popper manganite $La_{2-2x}Sr_{1+2x}Mn_2O_7$ by electrochemical F^- ion (de)intercalation[45]. However, this mechanism can be ruled out in our case, as it would result in an opposite F location according to the electric field applied for the polarization (**Fig. 5**). Another possibility is linked to the decomposition of PVDF, forming HF molecules that can be driven by the voltage. However, it can also be excluded because this type of decomposition is known to occur at temperatures higher than 400°C[46], where HF exists in a gaseous form. Thirdly, it is unlikely to move the highly electronegative (4.0) F atoms across the PVDF layer without interacting with other matter. We believe the most plausible scenario is that the C-F bond remains during the F motion, while the bond repeatedly breaks and re-bonds with another C driven by the electric field. A similar mechanism has been proposed for F atom diffusion on the Si(111) surface[47]. Unlike ionic motion in the non-organic magneto-ionic devices[35,36,45,48], atomic motion in organic structures can be mediated by carbon dangling bonds providing available sites for atomic diffusion. Additionally, the dipole associated with C-F bonds could induce the rotation of C-H chains

under an applied electric field, facilitating F motion across the PVDF layer. For a more in-depth discussion, please refer to **SI Note 14**.

It has been noted that the two resistance *vs.* polarizing voltage loops exhibit different coercivities, as illustrated in **Fig. 2b**. Specifically, we consistently observe that the coercivity voltage during the first cycle is larger than that in the second cycle. However, starting from the third cycle, the loops can well overlap with the second cycle. This suggests that during the first cycle measurement, more energy is required to initialize the motion of F through the PVDF layer. However, once the junction is activated, the motion of F becomes more facile, allowing it to follow the established path across the PVDF layer driven by the polarizing voltage.

3. Conclusions

In conclusion, we have successfully achieved a remarkably high tunneling magnetoresistance in an organic spintronic memristor, employing a novel memristive mechanism based on voltage-controlled fluorine motion. The exceptional performance demonstrated in both tunneling magnetoresistance and resistance change ratio promises the advancement of multifunctional devices, enabling the applications such as multi-level storage and plasticity-tunable artificial synapses for neuromorphic computing. In addition, the capability to control the sign and tune the amplitude of TMR through electrical polarization of the organic memristor is analog to the tunneling electro-magnetoresistance (TEMR) defined for MFTJ[49], which is a strongly desired property for electronic control of next-generation spintronic device applications. Moreover, the prospect of fabricating large-scale organic layers through low-cost, solution-based Langmuir-Blodgett processes makes these developments highly attractive for wearable, flexible, and implantable device applications[50].

Experimental Section/Methods

Sample Preparation: The LSMO/PVDF/Co/Au structures were fabricated with the following procedure. Initially, a 50 nm thick $La_{0.6}Sr_{0.4}MnO_3$ film was epitaxially grown on a (001)-oriented $SrTiO_3$ substrate using pulsed laser deposition (KrF laser 248 nm) at a deposition temperature of 750°C in a flowing oxygen atmosphere at 300 mTorr. Next, PVDF films were deposited using a vertical Langmuir-Blodgett method (KSV NIMA) as outlined below. We purchased PVDF beads from Sigma-Aldrich (Ref. 427152). The average M_w is ~180,000 g/mol determined by GPC, and the average M_n is ~71,000 g/mol. A small amount of solution with a concentration of 0.01 wt% of PVDF dissolved in dimethyl sulfoxide (DMSO) was dispersed onto the surface of an ultra-pure water subphase. The PVDF molecules were then compressed by slowly approaching two barriers until reaching a surface pressure of 5 mN/m. Subsequently, multiple PVDF layers were successively transferred to the substrate by vertically lifting the sample at a speed of 3 mm/min, waiting 30 minutes for each layer to dry. Following this, the PVDF film was annealed at 120ºC both in a glove box under an Ar atmosphere and in a molecular beam epitaxy (MBE) system under vacuum for 1 hour to eliminate the water and CO_2 contamination. Finally, 10 nm thick Co and 10 nm thick Au layers were deposited sequentially by e-beam evaporation in MBE, with the deposition carried out at 93 K to minimize the metal diffusion into the organic materials.

Two types of devices were fabricated. For the first type, schematically shown in **Fig. 2a**, the LSMO layer was initially etched using a diluted hydrogen chloride solution (37%) to create a 200 μm wide bar, serving as the bottom electrode. Five PVDF layers were then prepared by LB dip coating, with a nominal thickness of 5×2.2 nm=11 nm[27]. Subsequently, the top Co(10 nm)/Au (10 nm) electrode was deposited using an *in-situ* shadow mask. The resulting junction, schematically depicted in the inset of **Fig. 2a**, has a typical dimension of about 200×200 μm². For the second type of device, the LSMO bottom electrodes underwent UV lithography and ion milling processes to create junctions ranging in size from 5×5 to 40×40 μm² (Inset of **Fig. 3a**). Due to the reduction in junction size, a

thinner barrier of three PVDF layers was prepared. Following the deposition of the top Co/Au layers, UV lithography and ion milling were utilized again to fabricate the top electrodes (**Fig. 3a**). In both cases, 10 nm of Ti and 70 nm of Au were subsequently deposited on the LSMO and Co/Au electrodes to serve as bonding pads.

STEM-EELS characterization: HR-STEM coupled with spatially resolved EELS was conducted using a probe-corrected JEOL ARM200F microscope (cold FEG) equipped with a GATAN GIF quantum energy filter to reveal the structure and elemental distribution. The microscope was operated at 80 kV, and HAADF images were acquired during EELS mapping. EELS spectrum images were captured with a probe current of approximately 50 pA. Two EELS spectrum images were acquired simultaneously: one for the low-loss region containing the zero-loss and the other for the core loss. This method allows for advanced data post-processing, including energy drift correction and multiple scattering corrections. To enhance the quality of the STEM-EELS data, a multivariate statistical analysis software (temDM MSA) was employed to de-noise the core-loss spectrum image before processing the quantitative chemical maps[51]. Thin lamellas were fabricated through focused ion beam (FIB) milling using an FEI Helios Nanolab 600i dual-beam system.

AFM and PFM characterization: The surface morphology of the films was characterized using atomic force microscopy in tapping mode (TM-AFM) with an NX10 microscope (Park Systems, South Korea). Additionally, the local piezo-/ferroelectric behavior was probed utilizing the piezo-response mode of the AFM (PFM) on an MFP-3D AFM microscope (Asylum Research/Oxford Instruments, Santa Barbara, CA, USA), operating under ambient conditions. Switching spectroscopy PFM (SS-PFM) was employed in remnant mode by applying a continuous driving voltage V_{AC} of 2 V for PVDF/Au and 3 V for PVDF/LSMO, superimposed on an intermittent DC bias voltage between the conductive AFM tip and the grounded substrate. The off-field measurements yielded phase and amplitude piezo-response loops by promoting an electromechanical response against the electrostatic

interaction[52]. The dual AC resonance tracking (DART) mode of the PFM was utilized to enhance the low PFM signal. These analyses were conducted using a Pt/Ir-coated tip and a cantilever with a stiffness of approximately 1.9 $N \cdot m^{-1}$ (PPP-EFM, NanoSensors) as the nanometric conductive probe.

Magneto-transport measurement: For the device fabricated by an *in-situ* mask, the magneto-transport measurements were conducted using a liquid helium cooling cryostat. The temperature was varied from 10 K to 300 K and a magnetic field up to 3 kG was applied. *I-V* measurements were performed in two-terminal geometry using a Keithley 2450 as the voltage source and a Keithley 6487 picoammeter to measure the current. To polarize PVDF junction, electric voltage pulses with a ramp rate of 1 V/s and a duration of 1 s was applied to the junction with different voltage amplitude. The TMR is defined as: $TMR = \frac{R_{AP}-R_P}{R_P} \times 100\%$ for positive TMR, and $TMR = \frac{R_{AP}-R_P}{R_{AP}} \times 100\%$ for negative TMR, where R_P and R_{AP} represent the junction resistance when the magnetizations of the two electrodes are parallel and antiparallel, respectively.

For characterizing the magneto-transport properties of the small junctions fabricated using UV lithography, a physical property measurement system (EverCool-II, Quantum Design) was utilized to maintain a low-temperature environment. Pulsed voltage was generated using an arbitrary function generator (AFG 31000 Series, Tektronix), and the resistance was measured using a Keithley 2410 source meter. In the case of STDP characterization, a semiconductor parameter analyzer (4200A-SCS, Keithley, USA) was used to apply two programmable voltage spikes.

The *C-V* measurements were conducted at room temperature utilizing an HP4284 LCR meter, employing a sinusoidal voltage with an amplitude of 30 mV. The frequency range spanned from 200 Hz to 1 MHz.

Ab-initio calculations: Our first-principles calculations were conducted utilizing the projector-augmented wave (PAW) method[53], as implemented in the VASP package[54,55] with employing the

generalized gradient approximation[56]. To simulate the decomposed PVDF layer condition, we have utilized C-H chains without F, assuming that all F atoms have decomposed and diffused into the interface for the thin PVDF layer. For modeling the C-H chains, three monolayers of F-deprived PVDF chains were employed. The LSMO structure consists of a rock salt layer of $La_{0.5}Sr_{0.5}O$ on top of two layers of $LaSrMnO_3$. This Ruddlesden-Popper (RP) type structure of manganite is known to favor fluorine intercalation[45], which could also be attributed to the possible sub-stoichiometric condition on the LSMO surface. The LSMO/C-H chains interface was constructed by matching a 2×4 supercell of LSMO (001) (a=7.79 Å and b=3.91 Å) with a 1×3 supercell of C-H chains (a=8.58 Å, b=5.12 Å) on top. To model the insertion of F atoms into the LSMO surface, we have utilized a fluorinated phase of RP-type LSMO with an additional F layer at the LSMO/C-H interface. The other interface observed in the experimental samples was simulated using a (2×2×2.5) supercell of CoO (a=4.59 Å) matched with a (1×2) C-H chains. The magnetic ordering in CoO was set to antiferromagnetic type II, consistent with experiments[57] and theory[58]. To account for the localized d-orbitals in LSMO and CoO, we have adopted the GGA+U approach, including Hubbard U=4 eV, J=1 eV for the Mn-d orbitals, and U=5 eV, J=1 eV for the Co-d orbitals. In all calculations, the in-plane lattice constants were fixed to that of bulk LSMO. Atomic coordinates were relaxed until the forces became smaller than 1 meV/Å. A kinetic energy cutoff of 500 eV was employed for the plane-wave basis set, and the Γ point was used to sample the first Brillouin zone. To accurately describe the interaction of C-H chains with the substrate, van der Waals forces were incorporated using the Grimme type dispersion-corrected density functional theory-D2[59]. Finally, the spin-polarization of the DOS was calculated as $P_s = \frac{DOS^{majority} - DOS^{minority}}{DOS^{majority} + DOS^{minority}} \times 100\%$.

Acknowledgements

This work is supported by French National Research Agency (ANR) projects of FEOrgSpin (Grant No. ANR-18-CE24-0017), SIZMO2D (Grant No. ANR-19-CE24-0005) and SOTspinLED (Grant No. ANR-22-CE24-0006-01). We also acknowledge ICEEL (international) SHATIPN and CPER MatDS projects. Experiments were performed using equipment from the platforms CC-Davm and CC-MEM both funded by FEDER (EU), ANR, the Region Lorraine and the metropole of Grand Nancy. We also gratefully acknowledge the Chevreul Institute, the Ministère de l'Enseignement Supérieur, de la Recherche et de l'Innovation, the Region Hauts-de-France, the FEDER (EU), and the Major Domain Interest (DIM) "Eco-Energy Efficiency" of Artois University for equipment, in particular the MFP-3D microscope made available for PFM characterizations.

Author contributions

Y.L. coordinated the research project and designed the sample structure. C.L., Y.W. and X.L. prepared STO/LSMO substrates. A.N., T.C., Y.H., T.G., W.J., J.-C.L.B contributed to the optimization of PVDF preparations by AFM. A.N., P.T. and T.C. fabricated devices with in-situ mask. A.L.P designed the in-situ mask. Y.H., T.C. and L.B. developed devices with UV lithography. A.N., Y.L. and P.T. measured magneto-transport properties on the in-situ mask samples. Y.H., Y.W. and T.C. characterized magneto-transport properties on the lithographed samples. Y.W. and T.C. characterized the junction synaptic properties. T.C. and S.M. prepared STEM samples. X.D. performed STEM-EELS characterizations and analysis. K.D.F., A.D.C., A.F. and R.D. contributed to the AFM and PFM characterizations and interpretations. P.S. characterized C-V properties. F.I. and M.C. carried out *ab-initio* calculations. Y.L. prepared the manuscript, with the help of T.C., F.I., M.C., X.D., A.F., A.D.C., A.N. and Y.W. All authors analyzed the data, discussed the results and commented on the manuscript. A.N., T.C., F.I., Y.W and Y.H. contributed equally to this work.

Received: ((will be filled in by the editorial staff))
Revised: ((will be filled in by the editorial staff))
Published online: ((will be filled in by the editorial staff))

References:

[1] L. Chua. Memristor-The missing circuit element. *IEEE Transactions on Circuit Theory* **1971**, *18*, 507.

[2] F. Pan, S. Gao, C. Chen, C. Song, F. Zeng. Recent progress in resistive random access memories: Materials, switching mechanisms, and performance. *Materials Science and Engineering: R: Reports* **2014**, *83*, 1.

[3] T. Serrano-Gotarredona, T. Masquelier, T. Prodromakis, G. Indiveri, B. Linares-Barranco. STDP and STDP variations with memristors for spiking neuromorphic learning systems. *Frontiers in Neuroscience* **2013**, *7*, DOI 10.3389/fnins.2013.00002.

[4] S. H. Jo, T. Chang, I. Ebong, B. B. Bhadviya, P. Mazumder, W. Lu. Nanoscale memristor device as synapse in neuromorphic systems. *Nano Letters* **2010**, *10*, 1297.

[5] L. Gao, F. Alibart, D. B. Strukov. Programmable CMOS/memristor threshold logic. *IEEE Transactions on Nanotechnology* **2013**, *12*, 115.

[6] D. B. Strukov, G. S. Snider, D. R. Stewart, R. S. Williams. The missing memristor found. *Nature* **2008**, *453*, 80.

[7] H. Yildirim, R. Pachter. Mechanistic analysis of oxygen vacancy-driven conductive filament formation in resistive random access memory metal/NiO/metal structures. *ACS Applied Materials & Interfaces* 2018, *10*, 9802.

[8] J. J. Zhang, H. J. Sun, Y. Li, Q. Wang, X. H. Xu, X. S. Miao. AgInSbTe memristor with gradual resistance tuning. *Applied Physics Letters* **2013**, *102*, 183513.

[9] S. Z. Rahaman, S. Maikap, H.-C. Chiu, C.-H. Lin, T.-Y. Wu, Y.-S. Chen, P.-J. Tzeng, F. Chen, M.-J. Kao, M.-J. Tsai. Bipolar resistive switching memory using Cu metallic filament in Ge0.4Se0.6 solid electrolyte. *Electrochemical and Solid-State Letters* **2010**, *13*, DOI 10.1149/1.3339449.

[10] K. A. Campbell. Self-directed channel memristor for high temperature operation. *Microelectronics Journal* **2017**, *59*, 10.

[11] F. Alibart, S. Pleutin, D. Guérin, C. Novembre, S. Lenfant, K. Lmimouni, C. Gamrat, D. Vuillaume. An organic nanoparticle transistor behaving as a biological spiking synapse. *Advanced Functional Materials* **2010**, *20*, 330.

[12] S. M. Hus, R. Ge, P.-A. Chen, L. Liang, G. E. Donnelly, W. Ko, F. Huang, M.-H. Chiang, A.-P. Li, D. Akinwande. Observation of single-defect memristor in an MoS_2 atomic sheet. *Nature Nanotechnology* **2020**, *16*, 58.

[13] X. Wu, R. Ge, P. A. Chen, H. Chou, Z. Zhang, Y. Zhang, S. Banerjee, M. H. Chiang, J. C. Lee, D. Akinwande. Thinnest nonvolatile memory based on monolayer h-BN. *Advanced Materials* **2019**, *31*, 1806790.

[14] A. Chanthbouala, V. Garcia, R. O. Cherifi, K. Bouzehouane, S. Fusil, X. Moya, S. Xavier, H. Yamada, C. Deranlot, N. D. Mathur, M. Bibes, A. Barthélémy, J. Grollier. A ferroelectric memristor. *Nature Materials* **2012**, *11*, 860.

[15] C. Ma, Z. Luo, W. Huang, L. Zhao, Q. Chen, Y. Lin, X. Liu, Z. Chen, C. Liu, H. Sun, X. Jin, Y. Yin, X. Li. Sub-nanosecond memristor based on ferroelectric tunnel junction. *Nature Communications* **2020**, *11*, DOI 10.1038/s41467-020-15249-1.

[16] W. Huang, Y.-W. Fang, Y. Yin, B. Tian, W. Zhao, C. Hou, C. Ma, Q. Li, E. Y. Tsymbal, C.-G. Duan, X. Li. Solid-state synapse based on magnetoelectrically coupled memristor. *ACS Applied Materials & Interfaces* **2018**, *10*, 5649.

[17] P. Krzysteczko, J. Münchenberger, M. Schäfers, G. Reiss, A. Thomas. The memristive magnetic tunnel junction as a nanoscopic synapse-neuron system. *Advanced Materials* **2012**, *24*, 762.

[18] K. Singh, D. Kaur. Four logic states of tunneling magnetoelectroresistance in ferromagnetic shape memory alloy based multiferroic tunnel junctions. *Applied Physics Letters* **2017**, *111*, DOI 10.1063/1.4992795.

[19] M. Fang, S. Zhang, W. Zhang, J.-Q. Lu, E. Vetter, H. N. Lee, X. Xu, D. Sun, J. Shen. Nonvolatile multilevel states in multiferroic tunnel junctions. *Phys. Rev. Appl.* **2019**, *12*, DOI 10.1103/physrevapplied.12.044049.

[20] W. C. Huang, S. Yang, X. Li. Multiferroic heterostructures and tunneling junctions. *Journal of Materiomics* **2015**, *1*, 263.

[21] D. Pantel, S. Goetze, D. Hesse, M. Alexe. Reversible electrical switching of spin polarization in multiferroic tunnel junctions. *Nature Materials* **2012**, 11, 289.

[22] Y. Yin, J. Burton, Y. M. Kim, A. Y. Borisevich, S. J. Pennycook, S. M. Yang, T. W. Noh, A. Gruverman, X. G. Li, E. Y. Tsymbal, Q. Li. Enhanced tunnelling electroresistance effect due to a ferroelectrically induced phase transition at a magnetic complex oxide interface. *Nature Materials* **2013**, *12*, 397.

[23] A. J. Lovinger. Ferroelectric polymers. *Science* **1983**, *220*, 1115.

[24] T. Furukawa. Ferroelectric properties of vinylidene fluoride copolymers. *Phase Transitions* **1989**, *18*, 143.

[25] Y. Zhang, S. Mao, C. Jiang, B. Tian, C. Luo, H. Lin, J. Travas-sejdic, H. Peng, C.-G. Duan. Ferroelectric polarization assisted organic artificial synapse with enhanced performance. *Organic Electronics* **2022**, *109*, 106618.

[26] S. Kim, K. Heo, S. Lee, S. Seo, H. Kim, J. Cho, H. Lee, K.-B. Lee, J.-H. Park. Ferroelectric polymer-based artificial synapse for neuromorphic computing. *Nanoscale Horizons* **2021**, *6*, 139.

[27] B. B. Tian, J. L. Wang, S. Fusil, Y. Liu, X. L. Zhao, S. Sun, H. Shen, T. Lin, J. L. Sun, C. G. Duan, M. Bibes, A. Barthélémy, B. Dkhil, V. Garcia, X. J. Meng, J. H. Chu. Tunnel electroresistance through organic ferroelectrics. *Nature Communications* **2016**, *7*, DOI 10.1038/ncomms11502.

[28] S. Liang, H. Yang, H. Yang, B. Tao, A. Djeffal, M. Chshiev, W. Huang, X. Li, A. Ferri, R. Desfeux, S. Mangin, D. Lacour, M. Hehn, O. Copie, K. Dumesnil, Y. Lu. Ferroelectric control of organic/ferromagnetic spinterface. *Advanced Materials* **2016**, *28*, 10204.

[29] Z.-Z. Xiong, D. Wu, Z. V. Vardeny, J. Shi. Giant magnetoresistance in organic spin-valves. *Nature* **2004**, *427*, 821.

[30] F. Li, T. Li, F. Chen, F. Zhang. Excellent spin transport in spin valves based on the conjugated polymer with high carrier mobility. *Scientific Reports* **2015**, *5*, DOI 10.1038/srep09355.

[31] C. Xiao, H. Sun, L. Cheng, X. Devaux, A. Ferri, W. Huang, R. Desfeux, X.-G. Li, S. Migot, M. Chshiev, S. Rauf, Y. Qi, R. Wang, T. Zhang, C. Yang, S. Liang, Y. Lu. Temperature dependence of transport mechanisms in organic multiferroic tunnel junctions. *Journal of Physics D: Applied Physics* **2020**, *53*, 325301.

[32] S. Liang, Z. Yu, X. Devaux, A. Ferri, W. C. Huang, H. Yang, R. Desfeux, X. Li, S. Migot, D. Chaudhuri, H. Yang, M. Chshiev, C. Yang, B. Zhou, J. Fang, S. Mangin, Y. Lu. Quenching of spin polarization switching in organic multiferroic tunnel junctions by ferroelectric "ailing-channel" in organic barrier. *ACS Applied Materials & Interfaces* **2018**, *10*, 30614.

[33] Z. H. Xiong, D. Wu, Z. Valy Vardeny, J. Shi. Giant magnetoresistance in organic spin-valves. *Nature* **2004**, *427*, 821.

[34] F. Li, T. Li, F. Chen, F. Zhang. Excellent spin transport in spin valves based on the conjugated polymer with high carrier mobility. *Scientific Reports* **2015**, *5*, DOI 10.1038/srep09355.

[35] J. De Rojas, A. Quintana, A. F. Lopeandía, J. Salguero, B. Muñiz, F. Ibrahim, M. Chshiev, A. Nicolenco, M. O. Liedke, M. Butterling, A. Wagner, V. Sireus, L. Abad, C. Jensen, K. Li, J. Nogués, J. L. Costa-Krämer, E. Menéndez, J. Sort. Voltage-driven motion of nitrogen ions: a new paradigm for magneto-ionics. *Nature Communications* **2020**, *11*, DOI 10.1038/s41467-020-19758-x.

[36] M. Huang, M. U. Hasan, K. Klyukin, D. Zhang, D. Lyu, P. Gargiani, M. Valvidares, S. Sheffels, A. Churikova, F. Büttner, J. Zehner, L. Caretta, K.-Y. Lee, J. Chang, J.-P. Wang, K. Leistner, B. Yildiz, G. S. Beach. Voltage control of ferrimagnetic order and voltage-assisted writing of ferrimagnetic spin textures. *Nature Nanotechnology* **2021**, *16*, 981.

[37] S. Sanvito. The rise of spinterface science. *Nature Physics* **2010**, *6*, 562.

[38] M. Julliere. Tunneling between ferromagnetic films. *Physics Letters A* **1975**, *54*, 225.

[39] W. F. Brinkman, R. C. Dynes, J. M. Rowell. Tunneling conductance of asymmetrical barriers. *Journal of Applied Physics* **1970**, *41*, 1915.

[40] J. van Elp, J. L. Wieland, H. Eskes, P. Kuiper, G. A. Sawatzky, F. M. de Groot, T. S. Turner. Electronic structure of CoO, Li-doped CoO, and $LiCoO_2$. *Physical Review B* **1991**, *44*, 6090.

[41] N. Alidoust, M. Lessio, E. A. Carter. Cobalt (II) oxide and nickel (II) oxide alloys as potential intermediate-band semiconductors: A theoretical study. *Journal of Applied Physics* **2016**, *119*, 025102.

[42] Y. Lu, M. Tran, H. Jaffrès, P. Seneor, C. Deranlot, F. Petroff, J.-M. George, B. Lépine, S. Ababou, G. Jézéquel. Spin-polarized inelastic tunneling through insulating barriers. *Physical Review Letters* **2009**, *102*, DOI 10.1103/physrevlett.102.176801.

[43] M. Grünewald, N. Homonnay, J. Kleinlein, G. Schmidt. Voltage-controlled oxide barriers in organic/hybrid spin valves based on tunneling anisotropic magnetoresistance. *Physical Review B* **2014**, *90*, DOI 10.1103/physrevb.90.205208.

[44] S. Kumari, N. Mottaghi, C.-Y. Huang, R. Trappen, G. Bhandari, S. Yousefi, G. Cabrera, M. S. Seehra, M. B. Holcomb. Effects of oxygen modification on the structural and magnetic properties of highly epitaxial $La_{0.7}Sr_{0.3}MnO_3$ (LSMO) thin films. *Scientific Reports* **2020**, *10*, DOI 10.1038/s41598-020-60343-5.

[45] S. Vasala, A. Jakob, K. Wissel, A. I. Waidha, L. Alff, O. Clemens. Reversible tuning of magnetization in a ferromagnetic Ruddlesden-Popper-type manganite by electrochemical fluoride-ion intercalation. *Advanced Electronic Materials* **2019**, *6*, 1900974.

[46] M. C. Rehwoldt, Y. Wang, F. Xu, P. Ghildiyal, M. R. Zachariah. High-temperature interactions of metal oxides and a PVDF binder. *ACS Applied Materials & Interfaces* **2022**, *14*, 8938.

[47] Y. Asari, J. Nara, T. Ohno. Theoretical study on diffusion mechanism of fluorine atom adsorbed on Si(111) reconstructed surface. *Surface Science* **2011**, *605*, 225.

[48] A. J. Tan, M. Huang, C. O. Avci, F. Büttner, M. Mann, W. Hu, C. Mazzoli, S. Wilkins, H. L. Tuller, G. S. Beach. Magneto-ionic control of magnetism using a solid-state proton pump. *Nature Materials* **2018**, *18*, 35.

[49] V. Garcia, M. Bibès, L. Bocher, S. València, F. Kronast, A. Crassous, X. Moya, S. Enouz-Védrenne, A. Gloter, D. Imhoff, C. Deranlot, N. D. Mathur, S. Fusil, K. Bouzéhouane, A. Barthélémy. Ferroelectric control of spin polarization. *Science* **2010**, *327*, 1106.

[50] Y. Fujisaki, H. Koga, Y. Nakajima, M. Nakata, H. Tsuji, T. Yamamoto, T. Kurita, M. Nogi, N. Shimidzu. Transparent nanopaper-based flexible organic thin-film transistor array. *Advanced Functional Materials* **2013**, *24*, 1657.

[51] P. Potapov. Why principal component analysis of STEM spectrum-images results in “abstract”, uninterpretable loadings? *Ultramicroscopy* **2016**, *160*, 197.

[52] H. Qiao, D. Seol, C. Sun, Y. Kim. Electrostatic contribution to hysteresis loop in piezoresponse force microscopy. *Applied Physics Letters* **2019**, *114*, 152901.

[53] P. E. Blöchl. Projector augmented-wave method. *Physical Review B* **1994**, *50*, 17953.

[54] G. Kresse, J. Hafner. Ab initio molecular dynamics for liquid metals. *Physical Review B* **1993**, *47*, 558.

[55] G. Kresse, J. Furthmüller. Efficient iterative schemes forab initiototal-energy calculations using a plane-wave basis set. *Physical Review B* **1996**, *54*, 11169.

[56] J. P. Perdew, K. Burke, M. Ernzerhof. Generalized gradient approximation made simple. *Physical Review Letters* **1996**, *77*, 3865.

[57] W. L. Roth. Magnetic structures of MnO, FeO, CoO, and NiO. *Physical Review* **1958**, *110*, 1333.

[58] H.-X. Deng, J. Li, S.-S. Li, J.-B. Xia, A. Walsh, S.-H. Wei. Origin of antiferromagnetism in CoO: A density functional theory study. *Applied Physics Letters* **2010**, *96*, 162508.

[59] T. Bučko, J. Hafner, S. Lebègue, J. G. Ángyán. Improved description of the structure of molecular and layered crystals: Ab initio DFT calculations with van der Waals corrections. *The Journal of Physical Chemistry A* **2010**, *114*, 11814.

Table of content:

Summary: We discover the voltage-driven F motion in the $La_{0.6}Sr_{0.4}MnO_3$(LSMO) /poly (vinylidene fluoride) (PVDF) /Co junction, which can generate a huge reversible resistivity change up to 10^6% with *ns* timescale upon polarizing voltage. The removing F from PVDF layer also significantly enhances the tunneling magnetoresistance, paving the way to develop multifunctional organic spintronic memristor for storage and neuromorphic applications.